THE JOURNAL OF PHYSICAL CHEMISTRY C

Article

pubs.acs.org/JPCC

In Situ X-ray Diffraction Study of Co−Al Nanocomposites as Catalysts for Ammonia Decomposition

Ying-Qiu Gu,[†] Xin-Pu Fu,[†] Pei-Pei Du,[§] Dong Gu,[‡] Zhao Jin,[†] Yu-Ying Huang,[§] Rui Si,*[,§] Li-Qiang Zheng,[†] Qi-Sheng Song,[†] Chun-Jiang Jia,*[,†] and Claudia Weidenthaler*[,‡]

[†]Key Laboratory for Colloid and Interface Chemistry, Key Laboratory of Special Aggregated Materials, School of Chemistry and Chemical Engineering, Shandong University, Jinan 250100, China

[‡]Max-Planck-Institut für Kohlenforschung, Kaiser-Wilhelm-Platz 1, Mülheim an der Ruhr D-45470, Germany

[§]Shanghai Synchrotron Radiation Facility, Shanghai Institute of Applied Physics, Chinese Academy of Sciences, Shanghai 201204, China

Supporting Information

ABSTRACT: Co−Al nanocomposite materials as active and stable catalysts for ammonia decomposition have been synthesized by a one-pot evaporation-induced self-assembly method. The catalysts were characterized by various techniques including powder X-ray diffraction (XRD), X-ray absorption fine structure (XAFS), X-ray photoelectron spectroscopy (XPS), N_2 adsorption/desorption, and transmission/scanning electron microscopy (TEM/SEM). Especially, *in situ* XRD under catalytic reaction conditions was performed, and metallic Co with a cubic structure was identified to be most probably the active crystalline phase for the decomposition of ammonia; also, contribution of CoO to the catalytic activity cannot be excluded. Most importantly, the introduction of alumina can significantly suppress the agglomeration of the active metallic Co phase and thus maintain the high activity of the cobalt catalyst.

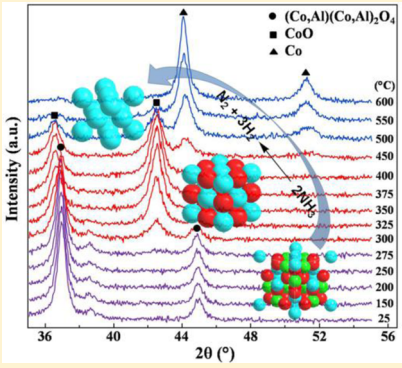

1. INTRODUCTION

In times of shortage of fossil fuels, scientists search for alternative energy carriers. For many years hydrogen has been discussed as one potential solution, but especially the complicated storage of hydrogen is one limiting factor for its broad applications. On the other hand, ammonia (NH_3) has been considered as an excellent hydrogen carrier due to its unique properties.[1−4] Ammonia provides a high H_2 storage capacity about 17 wt % hydrogen and also a high energy density compared with traditional carbonaceous materials. In addition, NH_3 can be easily liquefied under moderate conditions, getting transportation and storage more readily handled. The decomposition of ammonia is one way to generate CO_x-free hydrogen. Raising interest in NH_3 decomposition is motivated by the necessity for highly pure H_2 for proton exchange membrane fuel cells (PEMFCs) because CO_x, even in small amounts, would be poisonous to fuel cells.[5] Unconverted ammonia can be removed by using specific adsorbents such as Calgon-URC (Grace Davison grade 514).[6] Therefore, the catalytic generation of hydrogen from NH_3 decomposition is of both fundamental and practical importance.

Up to now, the best ammonia decomposition catalyst is Ru on carbon nanotubes.[2] However, NH_3 decomposition over various supported noble metals (e.g., Ru,[7−10] Ir,[11,12] Rh[13,14]) has the disadvantage of high costs, poor temperature stability, and difficulties for large-scale applications. Hence, it is necessary to develop less expensive catalysts based on nonprecious metals. As one alternative to noble metals, catalysts based on transition metals are considered.[15−22] In the past decades, Ni-,[15,16] Fe-,[17−21] and Mo-based[23,24] materials have been investigated as catalysts for NH_3 decomposition. However, most of the studied transition metal catalysts are mainly supported substances. The major disadvantage of supported catalysts is the low loading of the active species, thus resulting in low activities for NH_3 decomposition. On the other hand, the sintering effect will be severe if the active metal content is too high since NH_3 decomposition is a high temperature reaction. Hence, the controlled synthesis of novel transition metal catalysts with high contents of active species and a good catalytic performance for NH_3 decomposition is of both academic and practical interest in heterogeneous catalysis.

Cobalt-based catalysts have been used in heterogeneous catalysis including CO oxidation[25] and Fischer−Tropsch synthesis[26] but also for NH_3 decomposition.[27,28] However, high conversion was obtained only at temperatures above 600 °C. In addition, sintering of the catalyst particles is a severe problem especially during long operation times. To improve activity, the controlled synthesis of novel cobalt-based nanomaterials with high metal content and good thermal stability for the NH_3 decomposition reaction is of great demand. The

Received: March 27, 2015
Revised: June 9, 2015
Published: July 3, 2015

DOI: 10.1021/acs.jpcc.5b02932
J. Phys. Chem. C 2015, 119, 17102−17110

influence of Al on Co-containing catalysts with respect to catalytic performance is the focus of the present work. In this study, we report a one-pot evaporation-induced self-assembly method for the preparation of thermally stable Co−Al composite catalysts with different cobalt contents up to 90 at. %.

In order to design catalysts with better catalytic performance for NH_3 decomposition, it is very important to determine the catalytically active species, as well as the possible reaction pathways, by means of appropriate characterization techniques. Considering that NH_3 decomposition is a high-temperature reaction, most *in situ* methods for structural and/or surface analysis such as IR spectroscopy, X-ray photoelectron spectroscopy, or electron microscopy are difficult to use under such harsh reaction conditions. Nevertheless, *in situ* X-ray diffraction experiments were performed during NH_3 decomposition to monitor phase transformations, reduction processes, and microstructure changes of the different Co−Al composites.

2. EXPERIMENTAL METHODS

Preparation of Catalysts. Similar to mesoporous Al_2O_3 materials,[29] the Co−Al composite catalysts were prepared based on the evaporation-induced self-assembly procedure by using Pluronic P123 as a soft template. In a typical synthesis, 1.0 g of Pluronic P123 (M_{av} = 5800, $EO_{20}PO_{70}EO_{20}$, Sigma−Aldrich) was dissolved in ethanol (20 mL) at room temperature (RT). Citric acid ($C_6H_8O_7$, 0.84 g, Tianjin BoDi Chemicals) and appropriate quantities of $Al(NO_3)_3{\cdot}9H_2O$ and $Co(NO_3)_2{\cdot}6H_2O$ (Tianjin Kermal Chemicals) salts were added to the solution under vigorous stirring. The total amount of metal species (20 mmol) was kept constant, and the molar ratio of cobalt to aluminum was adjusted accordingly. The mixture was stirred at room temperature for 5 h and then transferred into a drying oven to undergo the solvent evaporation at 60 °C for another 2 days. The as-obtained product was calcined in air at 400 °C for 4 h with a slow ramping rate of 1 °C min^{-1} inside a tube oven. The air-calcined samples were labeled in the form of *X*CoAl, where *X*% means the atomic ratio of Co/(Co + Al).

Characterization. *Ex situ* X-ray diffraction (XRD) data were collected on a STOE STADI P transmission diffractometer using monochromatized Mo Kα_1 radiation. Data were collected with a position-sensitive detector (Dectris MYTHEN 1K) for 2θ ranging from 5° to 50°, with a step width of 0.03° and an acquisition time of 50 s per point. Crystal structure refinements were performed with the program package TOPAS 4.2.[30]

The X-ray absorption fine structure (XAFS) spectra were carried out at BL14W1 beamline of Shanghai Synchrotron Radiation Facility (SSRF) operated at 3.5 GeV under "top-up" mode with a current of 220 mA. The Co K-edge (E_0 = 7709 eV) XAFS data were collected in transmission mode by means of ion chambers. The energy was calibrated accordingly to the absorption edge measured for pure Co foil. Athena and Artemis codes were used to extract the data and fit the profiles. For the X-ray absorption near-edge structure (XANES) part, the experimental absorption coefficients as a function of energies $\mu(E)$ were processed by background subtraction and normalization procedures and reported as "normalized absorption". For the extended X-ray absorption fine structure (EXAFS) part, the Fourier transformed (FT) data in *R* space were analyzed by applying first shell approximation or Co_3O_4 model for fresh catalysts and Co model for used catalysts, respectively. The passive electron factors, S_0^2, were determined by fitting the experimental data obtained from a Co foil and fixing the Co−Co coordination number (CN) to be 12 and then fixing for further analysis of the measured samples. The parameters describing the electronic properties (e.g., correction to the photoelectron energy origin, E_0) and local structure environment including CN, bond distance (*R*), and Debye−Waller (D.W.) factor around the absorbing atoms were allowed to vary during the fit process. The fitted ranges for *k* and *R* spaces were selected to be *k* = 3−13 $Å^{-1}$ and *R* = 1.2−3.7 (Co−O) or 1.7−2.7 (Co−Co) Å (k^3 weighted), respectively.

The nitrogen sorption measurements were performed on an ASAP 2010 unit (Micromeritics) at 77 K after the activation of the samples at 200 °C for 4 h under vacuum. Pore size distribution curves were obtained by using the BJH method from the adsorption branch.

The transmission electron micrographs (TEMs) were obtained on a Hitachi HF 2000 microscope (200 kV). The high-resolution scanning electron microscope (HR-SEM) images and element mapping images, based on the energy-dispersive X-ray analysis (EDS) of the catalyst, were taken on a Hitachi S-5500 ultrahigh-resolution cold field emission scanning microscope at an acceleration voltage of 30 kV.

The X-ray photoelectron spectroscopy (XPS) measurements were performed with a Kratos HSi spectrometer with a hemispherical analyzer. The monochromatized Al X-ray source (*E* = 1486.6 eV) was operated at 15 kV and 15 mA. For the narrow scans, an analyzer pass energy of 40 eV was applied. The hybrid mode was used as a lens mode. The base pressure in the analysis chamber was 4×10^{-9} Torr. The binding energy scale was corrected for surface charging by use of the C 1s peak of contaminant carbon as a reference at 284.5 eV.

The *in situ* XRD experiments were performed using a reaction chamber (Anton Paar XRK900) mounted on a Bragg−Brentano diffractometer (PANalytical, X'Pert Pro, CuK_α: λ = 1.54056 Å, secondary monochromator). Data were collected for 2θ ranging from 35° to 55°, with a step width of 0.033°, and a counting time of 400 s per step. The samples (between 130 and 170 mg depending on the sample) were prepared in a MACOR sample holder (10 mm diameter, 1 mm depth) and heated from room temperature to 600 °C in a dry NH_3 atmosphere with a heating rate of 10 °C min^{-1}. First the samples were continuously heated from room temperature to 150 °C, and then temperature was increased by 50 °C for overview scans or by 25 °C for more detailed analysis. The flow of the reaction gas (space velocity) through the sample was set to a rate of 18 000 $cm^3\ g_{cat}^{-1}\ h^{-1}$. After the measurements, the catalyst was cooled from 600 °C to room temperature under a continuous N_2 flow. During the *in situ* diffraction experiments changes of the mean crystallite sizes of Co metal were calculated by the Scherrer equation. Due to the limited data quality a more precise domain size analysis by line profile methods was not applicable.

Catalytic Testing. For a typical NH_3 decomposition experiment, 50 mg (20−40 mesh) of the catalyst mixing with 200 mg of quartz sand (20−40 mesh) was loaded in a quartz tube (I.D. = 6 mm) fixed bed reactor, and pure gaseous NH_3 was passed through the catalyst bed. The concentrations of the outlet gases were analyzed by an online gas chromatograph (GC 9160, Shanghai OuHua), which is equipped with a thermal conductivity detector and Porapark N column (1.5 m of length). For the temperature-dependent conversion measurements of NH_3, the reactor temperature was increased from 400 to 700 °C in 50 °C steps. At each step, the reaction

DOI: 10.1021/acs.jpcc.5b02932
J. Phys. Chem. C 2015, 119, 17102−17110

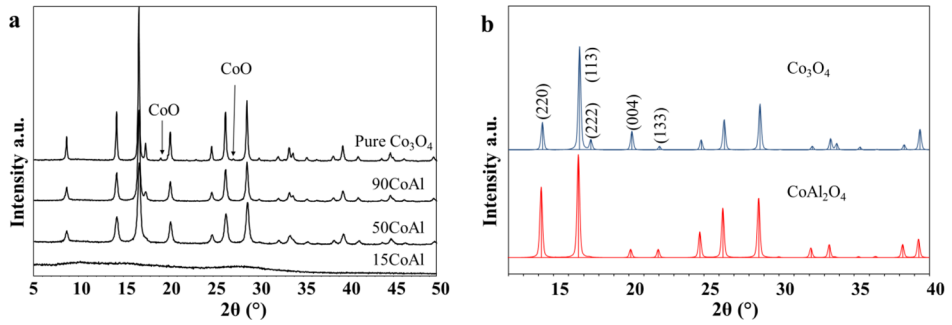

Figure 1. (a) XRD patterns of fresh Co−Al catalysts with different Co:Al ratios: pure Co_3O_4 , 90CoAl, 50CoAl, 15CoAl (bottom); (b) simulated powder patterns of pure Co_3O_4 (top, from ref 30) and $CoAl_2O_4$ (bottom, from ref 31).

Table 1. Crystalline Phases as Determined by XRD, Specific Surface Areas, and Co/Al Molar Ratio of Co−Al Catalysts as Obtained from XPS

	crystal phase		specific surface area (m^2 g^{-1})		Co/Al molar ratio (from XPS)
sample	fresh	used	fresh	used	fresh
15CoAl	Amorphous	Co	180	55	18/82
50CoAl	$(Co,Al)(Co,Al)_2O_4$	$(Co,Al)(Co,Al)_2O_4$, Co	113	83	39/61
90CoAl	$(Co,Al)(Co,Al)_2O_4$	Co	71	38	77/23
Pure Co	Co_3O_4/CoO	Co	20	<1	100/0

was allowed to equilibrate for 60 min to reach the steady-state conditions, and data obtained from the last gas chromatograph (GC) run at each temperature were used to calculate the conversion value. Blank tests with an empty reaction chamber yielded less than 1% conversion at 600 °C and 10% conversion at 700 °C. In order to evaluate the stability of the catalyst, the reaction temperature was maintained at 600 °C for 120 h, and the catalytic activity was recorded continuously.

3. RESULTS AND DISCUSSION

The crystalline phases of the Co−Al nanocomposites obtained after synthesis have been determined by XRD (Figure 1a and Table 1). It can be clearly seen that 15CoAl was noncrystalline, probably because of the existence of large amounts of amorphous alumina, while for samples without the addition of aluminum, the crystalline phase was highly crystalline Co_3O_4 (JCPDS card#: 42-1467) with smaller amounts of CoO as biphase (JCPDS card#: 48-1719). The analysis of the crystalline phases for medium concentrations (50−90 at. %) was more complicated since mixtures of pure Co_3O_4 and mixed spinel $CoAl_2O_4$ structures cannot be easily distinguished by XRD. Even though the lattice parameter of Co_3O_4 with 8.0850(9) Å are significantly smaller than the lattice parameter of $CoAl_2O_4$ (8.1047(4) Å), the qualitative analysis of the positions does not allow an assignment (Figure 1b). Nevertheless, a detailed crystal structure refinement of the crystalline compounds allows the assignment of the phase composition. The diffraction patterns of Co_3O_4 and $CoAl_2O_4$ show significant differences of several reflections such as (220), (222), and (133) (Figure 1b). This, on the other hand, allows distinguishing between both end-member compositions but also between mixed compositions between pure Co_3O_4 and pure $CoAl_2O_4$. Crystal structure refinements were performed for all crystalline samples, but here only the results obtained for sample 50CoAl will be discussed in more detail. The corresponding Rietveld refinements in Figure 2 reveal that the crystalline compound of sample 50CoAl corresponds to neither pure Co_3O_4 (Figure 2a) nor stoichiometric $CoAl_2O_4$

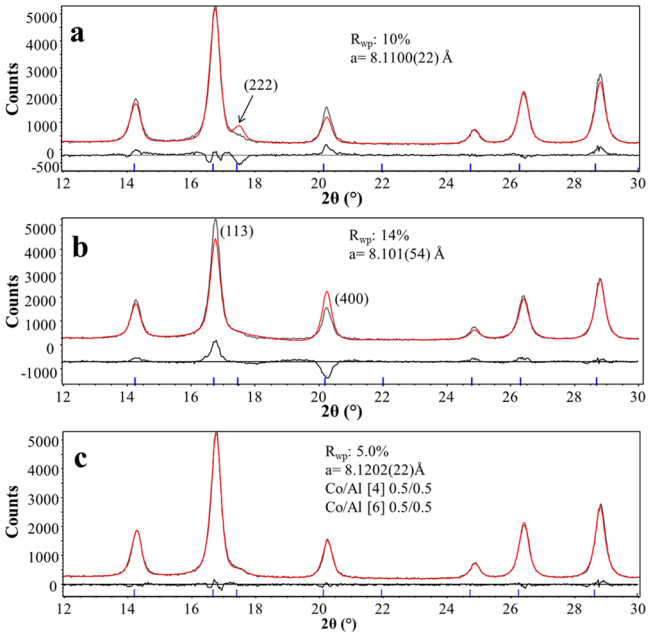

Figure 2. Rietveld refinement plots of the data collected for 50CoAl based on (a) pure Co_3O_4, (b) $CoAl_2O_4$, and (c) $(Co,Al)^{[4]}(Co,Al)^{[6]}{}_2O_4$. Red curves: experimental data. Blue curve: theoretical powder patterns. Gray curves: difference plot. The profile weighted residuals, R_{wp}, and the refined lattice parameters are given in the figures.

(Figure 2b). Structure refinement based on pure Co_3O_4 shows significant misfits between experimental and calculated data especially for the (222) and the (400) reflections. If the refinement is based on the structure model of $CoAl_2O_4$ with cation ordering of Co^{2+} on the tetrahedrally coordinated position and Al^{3+} on the octahedrally coordinated position, the refinement has even worse (Figure 2b). The deviations of the experimental data from the theoretical patterns indicate that the structure of the crystalline material does not belong to the pure structures. A much better fit is obtained, if both tetrahedral and

DOI: 10.1021/acs.jpcc.5b02932
J. Phys. Chem. C 2015, 119, 17102−17110

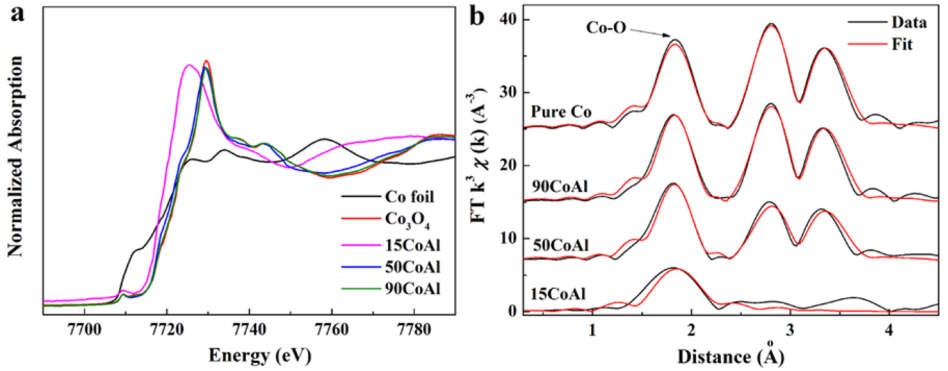

Figure 3. XANES profiles (a) and EXAFS *R* space (b) profiles of fresh Co−Al catalysts.

Table 2. EXAFS Fitting Results (*R*: Distance; CN: Coordination Number) of Fresh Co−Al Catalysts

	Co−O (First shell)		Co−Co (Second shell)		Co−Co (Third shell)	
sample	*R* (Å)	CN	*R* (Å)	CN	*R* (Å)	CN
15CoAl	1.93 ± 0.02	2.6 ± 0.6	–	–	–	–
50CoAl	1.94 ± 0.01	3.7 ± 0.3	2.89 ± 0.01	2.8 ± 0.4	3.39 ± 0.01	4.4 ± 0.6
90CoAl	1.94 ± 0.01	4.0 ± 0.2	2.88 ± 0.01	4.8 ± 0.4	3.39 ± 0.01	6.4 ± 0.6
Pure Co	1.93 ± 0.01	4.0 ± 0.3	2.88 ± 0.01	5.3 ± 0.7	3.39 ± 0.01	7.3 ± 0.9
Co_3O_4 model	1.943	4	2.874	6	3.370	6

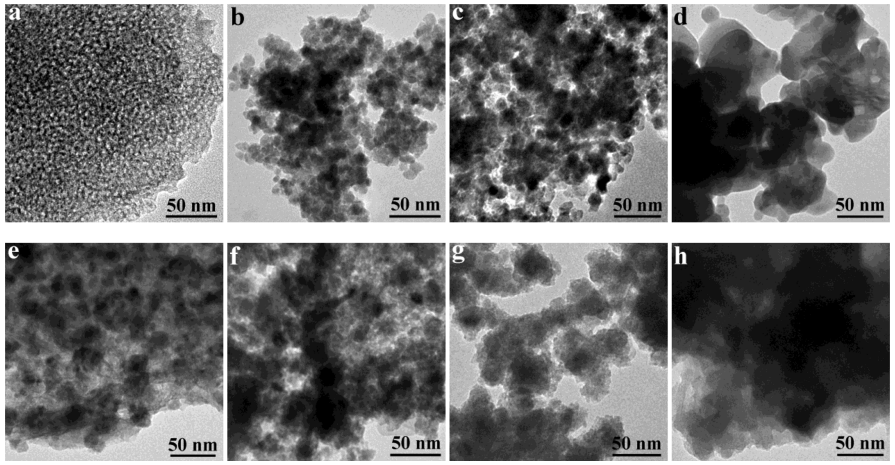

Figure 4. TEM images of the Co−Al catalysts before (a−d) and after (e−h) catalytic tests: (a, e) 15CoAl; (b, f) 50CoAl; (c, g) 90CoAl; (d, h) pure Co.

octahedral sites are occupied by Co and Al cations (Figure 2c). The refined occupancy factors reveal a 1:1 ratio of Co and Al on both positions, which refers perfectly to the ratio used for the synthesis. However, the distribution of Co with the oxidation states +2 and +3 on the octahedral site cannot be distinguished by structure refinements. Thus, the most probable crystalline phase has the composition $(Co,Al)[(Co,Al)_2O_4]$ (see Table 1).

The specific surface areas of the samples before and after catalytic testing are summarized in Table 1. With increasing Co content the specific surface areas of the samples analyzed before catalysis decrease. After catalytic testing all samples lost surface areas which is correlated to sintering of the particles. This is most severe for the pure Co sample, for which surface areas of less than 1 $m^2\ g^{-1}$ have been determined. Additionally, during removal of the samples from the reactors some of the samples react strongly exothermic if they come into contact with air which leads to an additional sintering and reoxidation of Co. This is also the reason why analyses of the reaction products after exposure to air with respect to surface areas and particle sizes may be of minor significance.

The X-ray absorption fine structure (XAFS) was further used to study the structural changes in the Co−Al composite catalysts with different Co contents. The X-ray absorption near-edge spectra (XANES) in Figure 3a exhibit that the cobalt structure in fresh samples is very similar to Co_3O_4, except for 15CoAl. Figure 3b displays the extended X-ray absorption fine structure (EXAFS) data on the Co−Al catalysts, as well as the simulation analysis. The corresponding fitting results in Table 2 clearly demonstrated the first shell of Co−O distance (*R*) centered at 1.93−1.94 Å with a coordination number (CN) of Co−O in 50−100 at. % Co was 3.7−4.0, which is in good agreement with the theoretical Co_3O_4 + $CoAl_2O_4$ model (CN = 4). For these Co−Al catalysts, the second and third shells of Co−Co can also be determined by the EXAFS fittings with the Co_3O_4 structural model (see Table 2). However, for 15CoAl,

DOI: 10.1021/acs.jpcc.5b02932
J. Phys. Chem. C 2015, 119, 17102−17110

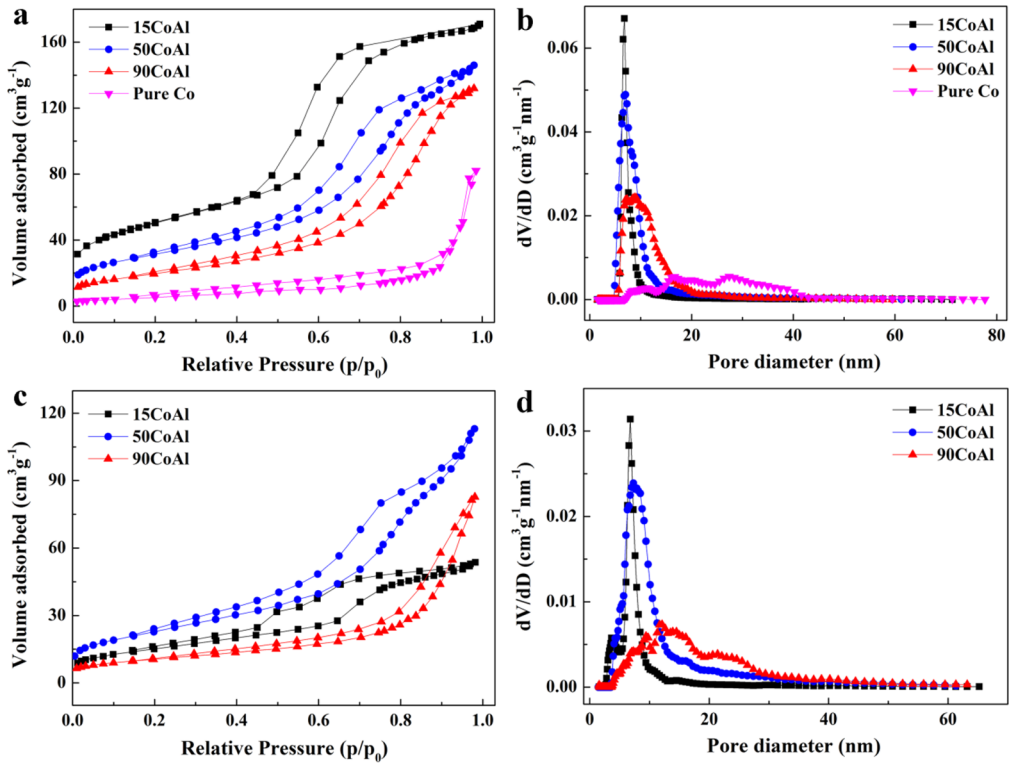

Figure 5. N_2 adsorption/desorption analysis: isotherms (a, c) and pore size distributions (b, d) of fresh (a, b) and used (c, d) Co−Al catalysts.

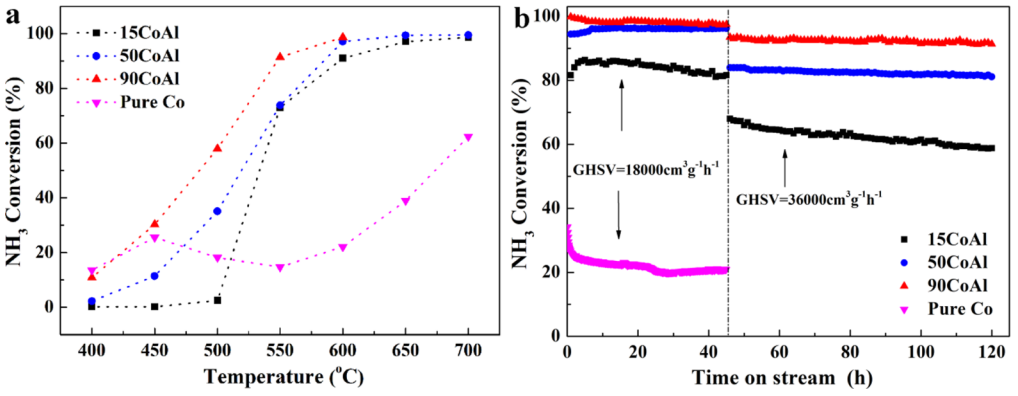

Figure 6. (a) Temperature-dependent NH_3 conversions at a gas hourly space velocity (GHSV) of 18 000 $cm^3\ g_{cat}^{-1}\ h^{-1}$ in the first cycle. (b) Long-term catalytic stability of the catalysts measured at 600 °C at different GHSV.

only the first shell of Co−O (1.93 Å, CN = 2.6) was identified due to its noncrystalline nature.

TEM investigation results exhibit that the fresh 15CoAl sample had a worm-like mesoporous structure, giving the uniform distribution of the bright regions (see Figure 4a). The corresponding N_2 adsorption/desorption with typical type IV isotherms with a H1 hysteresis loop shown in Figure 5a proves the presence of mesopores. The specific surface area of 180 $m^2\ g^{-1}$ (Table 1) is very high, and the pore size distribution is narrow (Figure 5b).

For high cobalt contents (50 and 90 at. %, Figures 4b,c) the porosity is low. These samples consisted of uniform nanoparticles with sizes between 15 and 20 nm as shown in the TEM images. The related N_2 adsorption/desorption data (type II isotherm) in Figure 5 and Table 1 also confirm a lower surface area and broader pore size distribution. However, for pure cobalt oxide, the particle size is 40 nm (Figure 4d), and the specific surface area is very low (20 $m^2\ g^{-1}$, Table 1). Thus, in this work, the introduction of mesoporous alumina to the cobalt oxide catalysts during chemical synthesis improved their textural properties. Furthermore, the XPS results show that for high Co contents (50−90 at. %, see Table 1) the molar ratios of Co:Al on the surface are smaller than that in the bulk phase. This indicates an enrichment of Al on the oxide surface.

The performances of catalysts with different Co:Al ratios are presented in Figure 6. For the temperature range between 400 and 600 °C a clear dependency of the catalytic activity from the Co content is observed. Comparing the conversion measured for different samples at the same reaction temperature, conversions are increased with increasing Co contents. For 90CoAl the conversion is among the highest ever reported for transition metal based catalysts (Table S1, Supporting Information). However, for pure Co_3O_4, the NH_3 conversion initially increased with increasing temperature up to 450 °C.

DOI: 10.1021/acs.jpcc.5b02932
J. Phys. Chem. C 2015, 119, 17102−17110

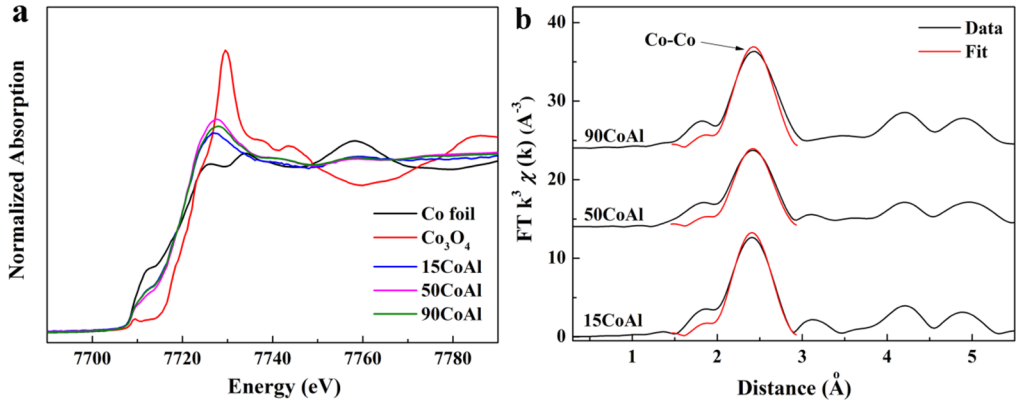

Figure 7. XANES profiles (a) and EXAFS *R* space (b) of Co−Al catalysts after catalytic tests.

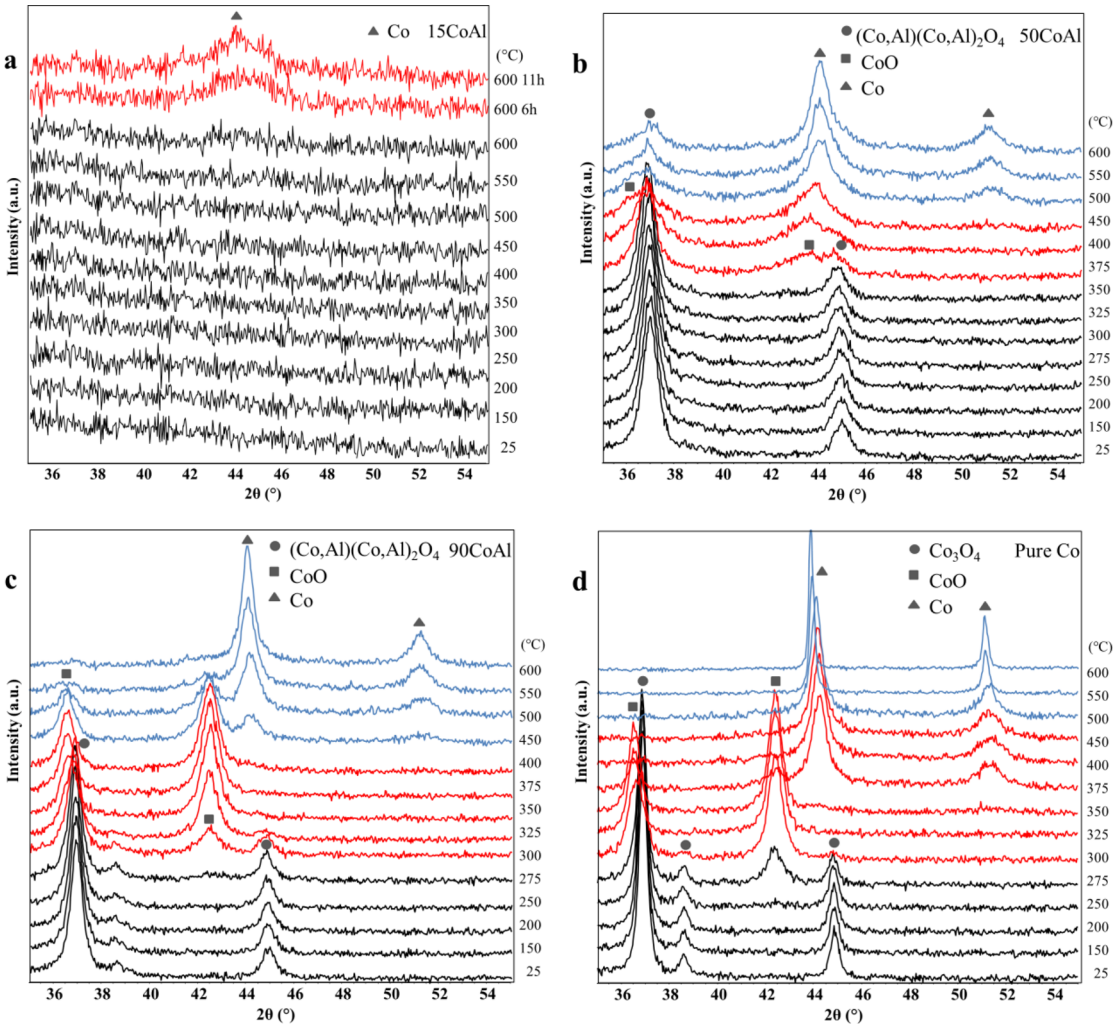

Figure 8. Stack plots of *in situ* XRD patterns collected under working conditions during the ammonia decomposition for (a) 15CoAl; (b) 50CoAl; (c) 90CoAl; and (d) pure Co_3O_4 without aluminum.

Then, conversion decreased during further temperature increase to 550 °C and finally increased again up to 700 °C. The initial increase from 400 to 450 °C was in agreement with the endothermic character of the NH_3 decomposition reaction, while the decreased conversion from 450 to 550 °C was mainly caused by the sintering of cobalt (Figure 8d). From 550 to 700 °C, temperature effect played the leading role, and NH_3 conversion increased again. To distinguish between the effect of temperature and of phase composition, the catalytic activity of each sample was tested in two identical cycles. After the first cycle, the catalysts were totally activated. Then the temperature was decreased to ambient temperature under NH_3 flow and increased again. The conversion data measured during the second cycle are shown in Figure S1 (Supporting Information). It can be seen that for Co−Al catalysts with Co contents up to 90 at. % the NH_3 conversion in the low temperature region

DOI: 10.1021/acs.jpcc.5b02932
J. Phys. Chem. C 2015, 119, 17102−17110

(400−500 °C) collected during the second cycle was higher than that obtained in the first cycle. For pure Co, no conversion is observed up to 600 °C before conversion reaches almost the same value at 700 °C which has been observed in the first cycle. Thermal decomposition as driving force for the decomposition cannot be excluded, but a blank test showed a much lower activity. For 95CoAl, NH_3 conversion in the second cycle was lower than that in the first cycle (Figure S2, Supporting Information), indicating agglomeration of the active Co phase occurred. For pure Co_3O_4, the NH_3 conversion in the second cycle was far lower than that observed for all Co−Al catalysts analyzed under the same reaction conditions. This may be explained by the absence of a strong interaction of cobalt with the alumina additives which seems to prevent sintering.

The long-term stability tests in Figure 6b display that the NH_3 conversion of 15CoAl reached 81% after the first 45 h (18 000 $cm^3\ g_{cat}^{-1}\ h^{-1}$) and gradually decreased to 58% during the sequential 75 h (36 000 $cm^3\ g_{cat}^{-1}\ h^{-1}$). The catalysts with cobalt contents of 50 at. % and 90 at. % were more active and stable than 15CoAl, with nearly constant NH_3 conversions throughout the whole reaction up to 120 h. In contrast, the pure cobalt oxide catalyst deactivated rapidly to only 21% conversion after the first 45 h period. Therefore, the addition of a small amount of aluminum of about 10 at. % significantly improved the stability of the active Co species and thus promoted reactivity of the Co−Al catalysts for NH_3 decomposition.

To investigate the effect of alumina, structural and textural characterizations on the used Co−Al catalysts after the NH_3 decomposition have been carried out. Due to the harsh reaction conditions up to 700 °C under high concentrations of ammonia and/or hydrogen, the morphology of 15CoAl obviously changed (Figure 4e). The mesoporous structure of the composite was transformed into a uniform nanostructure composed of small particles. The elimination of mesopores can also be identified by the N_2 adsorption/desorption results in Figure 5c and 5d, as well as by the significant decrease of the specific surface area from 180 to 55 $m^2\ g^{-1}$ (Table 1). No observable agglomeration occurred for samples 50CoAl and 90CoAl after the reaction (see Figure 4f,g), which correlates to their stability during the catalytic tests. Without addition of alumina, the pure cobalt oxide catalyst was severely sintered by forming large aggregates as can be seen in the TEM images (Figure 4h). This is linked to the loss of specific surface area (Table 1). The XANES spectra obtained for the used Co−Al catalysts are characteristic for Co(0) as compared to the spectrum of pure Co foil (Figure 7a). The minor profile mismatch near the edge jump could be due to the broadening effect caused by nanostructuring. The related EXAFS results (Figure 7b) obtained for the samples 15CoAl, 50CoAl, and 90CoAl after catalysis show Co−Co maxima at 2.51 Å which confirm the presence of metallic Co species in all three samples. The determined coordination numbers (CN) of the Co−Co shell are between 3.7 and 6.1. These values are significantly lower compared to that of bulk Co foil (CN = 12), which may be explained by the formation of very small nanoparticles as also observed by XRD (Figure 8).

As discussed above, the introduction of aluminum positively influenced the catalytic performance of Co-based materials for the ammonia decomposition reaction, thus raising the question about the nature of the active species. Therefore, *in situ* XRD measurements were performed, using similar reaction conditions as used for the catalytic test performed in the plug-flow reactor. A selection of *in situ* XRD patterns is summarized in Figure 8.

For 15CoAl (see Figure 8a), no crystalline components were formed up to 600 °C. After keeping the sample at 600 °C for longer time (5 h), a very broad peak corresponding to metallic Co appeared, and after 11 h at 600 °C the intensity has increased due to crystal growth. For the sample containing 50 at. % cobalt, a mixed spinel structure $(Co,Al)(Co,Al)_2O_4$ was the major crystalline phase up to 350 °C (Figure 8b). New reflections assigned to CoO appeared at 375 °C. However, the NH_3 conversion was below 3%. At 450 °C (11% conversion), more CoO and a small amount of metallic Co were generated. Further increase of the reaction temperature to 500 °C led to the formation of more metallic Co(0) (74% conversion). For the 50CoAl sample even at 600 °C (97% conversion), small amounts of the $(Co,Al)(Co,Al)_2O_4$ component could be detected. The cubic metallic Co phase with a crystallite size of about 6 nm was stable during reaction for 11 h at 600 °C.

For 90CoAl (see Figure 8c), the $(Co,Al)(Co,Al)_2O_4$ structure was much more instable and disappeared completely already above 350 °C. Intermediate CoO formed between 250 and 300 °C and was further transformed into metallic Co above 450 °C (30% conversion). The reduction of CoO to Co was completed at 550 °C (91% conversion), and full conversion was reached at 600 °C. After reaction for 11 h at 600 °C, the mean crystallite size of Co as determined form the *in situ* XRD data was 10 nm.

Without the addition of alumina, the reduction of pure Co_3O_4 to CoO began between 250−275 °C, and the sequential transformation from CoO to Co started above 350 °C (see Figure 8d). Metallic Co was the only crystalline phase at 400 °C. The crystal size increased rapidly from 10 nm at 400 °C to 40 nm at 550 °C and finally to 100 nm at 600 °C. Further sintering to a larger crystallite cannot be analyzed by XRD since significant peak broadening is only visible from crystallites <100 nm. Pronounced sintering could be one reason to explain the unusual catalytic behavior of pure cobalt oxide as shown in Figure 6a.

On the basis of the *in situ* XRD results, which are also supported by the XAFS, TEM, and N_2 adsorption/desorption data, there is strong evidence which crystalline phase is responsible for the catalytic activity of the NH_3 decomposition:

(1) The catalytic activity is significantly increased at the moment when metallic Co(0) is formed. Therefore, metallic cobalt is most probably the active species for the decomposition reaction, while $(Co,Al)(Co,Al)_2O_4$ (except pure Co_3O_4 catalyst) is the starting phase and CoO an intermediate compound. The conclusion that the increase of the catalytic activity is correlated to the complete reduction of the transition metal is similar to the results reported for Fe-based catalysts.[20] However, for Fe the formation of iron nitrides takes place in the temperature region between 500 and 650 °C before metallic Fe is formed. For Mo-based catalysts, different molybdenum nitrides form from the oxide precursor, and no Mo metal is observed.

Interestingly, during catalysis the mixed spinel structure starts to segregate into a crystalline Co oxide, whereas the Al-containing phase becomes amorphous. Figure 9 shows the comparison of the *in situ* XRD patterns for all Co−Al catalysts except 15CoAl collected at 500 °C. 90CoAl contains both metallic Co (11 nm) and CoO (9 nm) and exhibited the highest activity of 60% conversion at 500 °C. Pure Co_3O_4 catalyst without Al incorporation contains only metallic Co

DOI: 10.1021/acs.jpcc.5b02932
J. Phys. Chem. C 2015, 119, 17102−17110

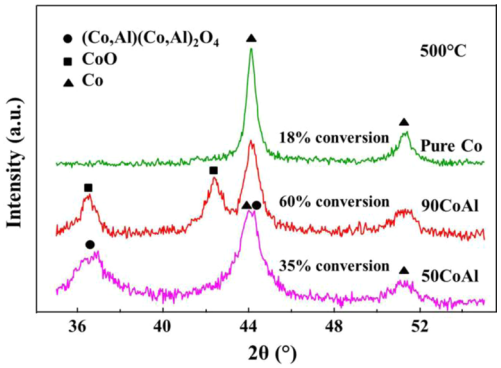

Figure 9. Comparison of *in situ* XRD patterns at 500 °C for the Co–Al catalysts with various Co contents.

with a mean crystallite size of about 15 nm. However, it has a much lower activity than measured for 90CoAl. Therefore, it would be too simple to correlate the good activity only to the phase composition of the catalyst. The experimental data reveal that many factors, including the active phase, domain size, surface species/area, and interaction between Co and Al_2O_3 could influence the activity of Co–Al samples. It should be mentioned that the aluminum-containing phase remains in an amorphous state during the reaction process. Also, at temperatures below 550 °C, the contribution of CoO to the catalytic activity cannot be excluded, although CoO is metastable during the reaction.

(2) Nanosized Co is active, while large-sized Co is much less active. For all samples, the specific surface areas are significantly reduced during the catalytic reaction (Table 1). *In situ* XRD indicates that sintering of the Co phase strongly depends on the aluminum content. This explains the reduction of the specific surface areas. However, the specific surface areas are still high, which is mainly due to the presence of an amorphous alumina phase. In addition to the size effect, the NH_3 conversion increases with increasing cobalt concentration. However, for pure Co_3O_4, severe sintering is detected, which leads to large crystallite sizes and a very low specific surface area. This influences the catalytic activity negatively. On the other hand, 15CoAl, though this sample contained the smallest crystallites of all samples (see Figure 4a), did not show a good catalytic performance, which may be due to the strong interaction between Co and Al_2O_3 and/or the small amount of Co.

(3) Small amounts of alumina (ca. 10 at. %) seem to be advantageous to stabilize the active Co nanoparticles. In this work, the initial mesoporous structure obtained during the formation of the cobalt–alumina composite is important in order to provide a good catalytic performance. The amorphous alumina phase formed during the reaction is effective in the stabilization of nanosized cobalt oxide particles. To provide further insight into the microstructure of the used catalyst, high-resolution SEM investigations were performed on sample 90CoAl after the ammonia decomposition. Typical SEM images and the corresponding selected area element maps (Co and Al) are shown in Figure 10a–c. It is demonstrated that Co and Al are uniformly dispersed; no Co- or Al-enriched regions were observed. All results shown so far indicate that the alumina component plays an important role during the ammonia decomposition reaction as an antisintering component.

4. CONCLUSION

In this study, Co–Al nanocomposite catalysts with different cobalt contents have been tested as catalysts for NH_3 decomposition. A small amount of Al (ca. 10 at. %) can significantly improve the stability of the Co catalyst via suppressing agglomeration, which helps the catalysts keep high activity even during long-term tests. The *in situ* XRD experiments showed that the stepwise reduction of the cobalt aluminum spinel $(Co,Al)(Co,Al)_2O_4$ to CoO and further to metallic Co is significantly influenced by the original Co content. With increasing cobalt content, the starting temperature of the reduction of $(Co,Al)(Co,Al)_2O_4$ to CoO is decreased. From the combination of the *in situ* XRD measurements with catalytic tests it is found, that besides metallic Co, CoO cannot be excluded to be an active phase for the ammonia decomposition reaction. The results obtained from all experimental data are helpful to expand the new design and/or synthesis routes toward highly active and thermally stable catalysts also useful for other heterogeneously catalyzed reactions.

■ ASSOCIATED CONTENT

Supporting Information

Figures S1 and S2 and Table S1. The Supporting Information is available free of charge on the ACS Publications website at DOI: 10.1021/acs.jpcc.5b02932.

■ AUTHOR INFORMATION

Corresponding Authors

*E-mail: sirui@sinap.ac.cn.
*E-mail: jiacj@sdu.edu.cn.
*E-mail: claudia.weidenthaler@mpi-mail.mpg.de.

Notes

The authors declare no competing financial interest.

■ ACKNOWLEDGMENTS

We thank Prof. Ferdi Schüth for the helpful suggestion and fruitful discussions, also Mr. Jan Ternieden for technical XRD support (Max-Planck-Institut für Kohlenforschung). Financial support from the National Science Foundation of China

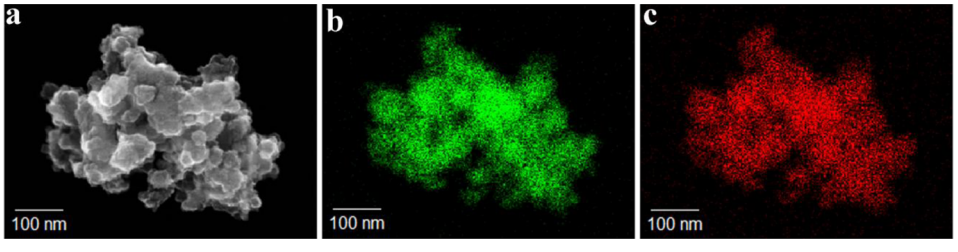

Figure 10. SEM image (a) and corresponding images of selected area element mapping (b: Co, c: Al) for the used 90CoAl catalyst.

DOI: 10.1021/acs.jpcc.5b02932
J. Phys. Chem. C 2015, 119, 17102–17110

(NSFC) (grant nos. 21301107, 21373259, and 11079005), Fundamental Research Funding of Shandong University (grant nos. 2014JC005), the Taishan Scholar Project of Shandong Province (China), the Hundred Talents Project of the Chinese Academy of Sciences, the Strategic Priority Research Program of the Chinese Academy of Sciences (grant no. XDA09030102), and the Max-Planck Society is acknowledged.

REFERENCES

(1) Schüth, F.; Palkovits, R.; Schlögl, R.; Su, D. S. Ammonia as a Possible Element in an Energy Infrastructure: Catalysts for Ammonia Decomposition. *Energy Environ. Sci.* **2012**, *5*, 6278−6289.
(2) Yin, S. F.; Xu, B. Q.; Zhou, W. P.; Au, C. T. A Mini-Review on Ammonia Decomposition Catalysts for On-site Generation of Hydrogen for Fuel Cell Applications. *Appl. Catal., A* **2004**, *277*, 1−9.
(3) Durbin, D. J. D.; Malardier-Jugroot, C. Density Functional Theory Analysis of Metal/Graphene Systems As a Filter Membrane to Prevent CO Poisoning in Hydrogen Fuel Cells. *J. Phys. Chem. C* **2011**, *115*, 808−815.
(4) Metkemeijer, R.; Achard, P. Ammonia as a Feedstock for a Hydrogen Fuel Cell; Reformer and Fuel Cell Behaviour. *J. Power Sources* **1994**, *49*, 271−282.
(5) Choudhary, T. V.; Goodman, D. W. CO-Free Production of Hydrogen via Stepwise Steam Reforming of Methane. *J. Catal.* **2000**, *192*, 316−321.
(6) Tang, J. M.; Jensen, K.; Waje, M.; Li, W.; Larsen, P.; Pauley, K.; Chen, Z.; Ramesh, P.; Itkis, M. E.; Yan, Y.; et al. High Performance Hydrogen Fuel Cells with Ultralow Pt Loading Carbon Nanotube Thin Film Catalysts. *J. Phys. Chem. C* **2007**, *111*, 17901−17904.
(7) Choudhary, T. V.; Sivadinarayana, C.; Goodman, D. W. Catalytic Ammonia Decomposition: CO_x-Free Hydrogen Production for Fuel Cell Applications. *Catal. Lett.* **2001**, *72*, 197−201.
(8) Yin, S. F.; Zhang, Q. H.; Xu, B. Q.; Zhu, W. X.; Ng, C. F.; Au, C. T. Investigation on the Catalysis of CO_x-Free Hydrogen Generation from Ammonia. *J. Catal.* **2004**, *224*, 384−396.
(9) Zhang, B.; Ni, X.; Zhang, W.; Shao, L.; Zhang, Q.; Girgsdies, F.; Liang, C.; Schlögl, R.; Su, D. S. Structural Rearrangements of Ru Nanoparticles Supported on Carbon Nanotubes Under Microwave Irradiation. *Chem. Commun.* **2011**, *47*, 10716−10718.
(10) Karim, A. M.; Prasad, V.; Mpourmpakis, G.; Lonergan, W. W.; Frenkel, A. I.; Chen, J. G.; Vlachos, D. G. Correlating Particle Size and Shape of Supported Ru/γ-Al_2O_3 Catalysts with NH_3 Decomposition Activity. *J. Am. Chem. Soc.* **2009**, *131*, 12230−12239.
(11) Chen, W.; Ermanoski, I.; Madey, T. E. Decomposition of Ammonia and Hydrogen on Ir Surfaces: Structure Sensitivity and Nanometer-Scale Size Effects. *J. Am. Chem. Soc.* **2005**, *127*, 5014−5015.
(12) García-García, F. R.; Guerrero-Ruiz, A.; Rodríguez-Ramos, I.; Goguet, A.; Shekhtman, S. O.; Hardacre, C. TAP Studies of Ammonia Decomposition Over Ru and Ir Catalysts. *Phys. Chem. Chem. Phys.* **2011**, *13*, 12892−12899.
(13) Leewis, C. M.; Kessels, W. M. M.; van de Sanden, M. C. M.; Niemantsverdriet, J. W. Ammonia Adsorption and Decomposition on Silica Supported Rh Nanoparticles Observed by *in situ* Attenuated Total Reflection Infrared Spectroscopy. *Appl. Surf. Sci.* **2006**, *253*, 572−580.
(14) Chmielarz, L.; Jablonska, M.; Struminski, A.; Piwowarska, Z.; Wegrzyn, A.; Witkowski, S.; Michalik, M. Selective Catalytic Oxidation of Ammonia to Nitrogen Over Mg-Al, Cu-Mg-Al and Fe-Mg-Al Mixed Metal Oxides Doped with Noble Metals. *Appl. Catal., B* **2013**, *130*, 152−162.
(15) Zhang, J.; Xu, H.; Jin, X.; Ge, Q.; Li, W. Characterizations and Activities of the Nano-sized Ni/Al_2O_3 and Ni/La-Al_2O_3 Catalysts for NH_3 Decomposition. *Appl. Catal., A* **2005**, *290*, 87−96.
(16) Liu, H.; Wang, H.; Shen, J.; Sun, Y.; Liu, Z. Preparation, Characterization and Activities of the Nano-sized Ni/SBA-15 Catalyst for Producing CO_x-free Hydrogen from Ammonia. *Appl. Catal., A* **2008**, *337*, 138−147.
(17) Zhang, J.; Comotti, M.; Schüth, F.; Schlögl, R.; Su, D. S. Commercial Fe- or Co-containing Carbon Nanotubes as Catalysts for NH_3 Decomposition. *Chem. Commun.* **2007**, 1916−1918.
(18) Zhang, J.; Müller, J. O.; Zheng, W.; Wang, D.; Su, D.; Schlögl, R. Individual Fe−Co Alloy Nanoparticles on Carbon Nanotubes: Structural and Catalytic Properties. *Nano Lett.* **2008**, *8*, 2738−2743.
(19) Lu, A.-H.; Nitz, J.-J.; Comotti, M.; Weidenthaler, C.; Schlichte, K.; Lehmann, C. W.; Terasaki, O.; Schüth, F. Spatially and Size Selective Synthesis of Fe-Based Nanoparticles on Ordered Mesoporous Supports as Highly Active and Stable Catalysts for Ammonia Decomposition. *J. Am. Chem. Soc.* **2010**, *132*, 14152−14162.
(20) Feyen, M.; Weidenthaler, C.; Güttel, R.; Schlichte, K.; Holle, U.; Lu, A.-H.; Schüth, F. High-Temperature Stable, Iron-Based Core−Shell Catalysts for Ammonia Decomposition. *Chem. - Eur. J.* **2011**, *17*, 598−605.
(21) Pelka, R.; Kiełbasa, K.; Arabczyk, W. Catalytic Ammonia Decomposition during Nanocrystalline Iron Nitriding at 475 °C with NH_3/H_2 Mixtures of Different Nitriding Potentials. *J. Phys. Chem. C* **2014**, *118*, 6178−6185.
(22) Zheng, W.; Cotter, T. P.; Kaghazchi, P.; Jacob, T.; Frank, B.; Schlichte, K.; Zhang, W.; Su, D. S.; Schüth, F.; Schlögl, R. Experimental and Theoretical Investigation of Molybdenum Carbide and Nitride as Catalysts for Ammonia Decomposition. *J. Am. Chem. Soc.* **2013**, *135*, 3458−3464.
(23) Tagliazucca, V.; Schlichte, K.; Schüth, F.; Weidenthaler, C. Molybdenum-based Catalysts for the Decomposition of Ammonia: In situ X-ray Diffraction Studies, Microstructure, and Catalytic Properties. *J. Catal.* **2013**, *305*, 277−289.
(24) Tagliazucca, V.; Leoni, M.; Weidenthaler, C. Correction: Crystal Structure and Microstructural Changes of Molybdenum Nitrides Traced During Catalytic Reaction by in situ X-ray Diffraction Studies. *Phys. Chem. Chem. Phys.* **2014**, *16*, 6182−6188.
(25) Jia, C.-J.; Schwickardi, M.; Weidenthaler, C.; Schmidt, W.; Korhonen, S.; Weckhuysen, B. M.; Schüth, F. Co_3O_4−SiO_2 Nanocomposite: A Very Active Catalyst for CO Oxidation with Unusual Catalytic Behavior. *J. Am. Chem. Soc.* **2011**, *133*, 11279−11288.
(26) Melaet, G.; Ralston, W. T.; Li, C.-S.; Alayoglu, S.; An, K.; Musselwhite, N.; Kalkan, B.; Somorjai, G. A. Evidence of Highly Active Cobalt Oxide Catalyst for the Fischer−Tropsch Synthesis and CO_2 Hydrogenation. *J. Am. Chem. Soc.* **2014**, *136*, 2260−2263.
(27) Frenkel, A. I.; Wang, Q.; Marinkovic, N.; Chen, J. G.; Barrio, L.; Si, R.; Cámara, A. L.; Estrella, A. M.; Rodriguez, J. A.; Hanson, J. C. Combining X-ray Absorption and X-ray Diffraction Techniques for in Situ Studies of Chemical Transformations in Heterogeneous Catalysis: Advantages and Limitations. *J. Phys. Chem. C* **2011**, *115*, 17884−17890.
(28) Pistor, P.; Borchert, J.; Fränzel, W.; Csuk, R.; Scheer, R. Monitoring the Phase Formation of Coevaporated Lead Halide Perovskite Thin Films by in Situ X-ray Diffraction. *J. Phys. Chem. Lett.* **2014**, *5*, 3308−3312.
(29) Yuan, Q.; Yin, A. X.; Luo, C.; Sun, L. D.; Zhang, Y. W.; Duan, W. T.; Liu, H. C.; Yan, C. H. Facile Synthesis for Ordered Mesoporous γ-Aluminas with High Thermal Stability. *J. Am. Chem. Soc.* **2008**, *130*, 3465−3472.
(30) Will, G.; Masciocchi, N.; Parrish, W.; Hart, M. Refinement of Simple Crystal Structures from Synchrotron Radiation Powder Diffraction Data. *J. Appl. Crystallogr.* **1987**, *20*, 394−401.
(31) Bosi, F.; Hålenius, U.; D'Ippolito, V.; Andreozzi, G. B. Blue Spinel Crystals in the $MgAl_2O_4$-$CoAl_2O_4$ Series: Cation Ordering over Short Range and Long Range Scales. *Am. Mineral.* **2012**, *97*, 1834−1840.

DOI: 10.1021/acs.jpcc.5b02932
J. Phys. Chem. C 2015, 119, 17102−17110